Convolution Based Techniques for Computing Self Attraction and Loading in MOM6

Anthony Chen[1,6], He Wang[2,3,4], Brian K. Arbic[2,5], and Robert Krasny[1]

[1]Department of Mathematics, University of Michigan, Ann Arbor, MI, USA
[2]Department of Earth and Environmental Sciences, University of Michigan, Ann Arbor, MI, USA
[3]UCAR, Boulder, CO, USA
[4]NOAA-GFDL, Princeton, NJ, USA
[5]Research School of Earth Sciences, Australian National University, Canberra, ACT, Australia
[6]Department of Mathematics, National University of Singapore, Singapore

Correspondence: Anthony Chen (cygnari@umich.edu)

Abstract. Self Attraction and Loading (SAL), which ~~includes~~ accounts for the deformation of the solid Earth under the load of the ocean tide and the self-gravitation of the so-deformed Earth as well as of the ocean tides themselves, is an important ~~term~~ effect to include in numerical models of the ocean tides. Computing ~~SAL~~ the SAL potential and its gradient is a challenging problem that is ~~usually tackled using spherical harmonics. The spherical harmonic approach has several~~ often accomplished using the spherical harmonics transform (SHT), but that approach has drawbacks which limit its accuracy. ~~In this work , we propose an alternative technique based on a spherical convolution . We implement the convolution technique~~ This work employs an alternative approach based on computing the spherical convolution integral, which utilizes an approximate SAL Green's function and is accelerated by the recently developed Cubed Sphere Fast Multipole Method (CSFMM). The convolution technique is implemented in the Modular Ocean Model, version 6, ~~and demonstrate that it allows for~~ where it provides more accurate tides than those obtained with the SHT when measured against tidal datasets based ~~upon~~ on satellite altimetry. ~~The convolution based SAL reduces the error by reducing spurious oscillations associated with the Gibbs phenomenon. These oscillations are large in coastal regions under the traditional spherical harmonic approach~~Previous investigators have cited Gibbs phenomenon as a possible source of error in SHT calculations, but our application of Cesàro summation to the SHT failed to reduce the error, which suggests that other errors are also significant, such as aliasing error due to finite grid resolution, and finite difference errors in computing the gradient of the SAL potential. The convolution approach has different sources of error including errors in the approximate SAL Green's function, quadrature error in computing the convolution integral, and interpolation error from the CSFMM. In addition to comparing the accuracy of the two approaches, we also present the runtime for parallel calculations using up to 1024 MPI ranks.

1 Introduction

Tides are an important component of the Earth system. In many open-ocean and coastal regions, tides ~~are a critical component of~~ dominate sea level and/or current variability. Tides are also implicated as a major ~~component of~~ element in the ocean

mixing cycle, which contributes significantly to the background oceanic stratification in both the coastal and ~~pelagic ocean (Simpson and Hunter (1974); Munk and Wunsch (1998))~~open ocean (Simpson and Hunter, 1974; Munk and Wunsch, 1998). Tides are a result of astronomical gravitational forcing, and this tidal forcing drives periodic changes in the sea surface height (SSH) and ~~in~~ the currents. ~~An~~ Hence an improved understanding of ~~the tides is important for deepening our understanding of the oceans and~~ tidal dynamics is necessary for developing improved models.

Historically, tides were independently modeled from the rest of the ocean, primarily in barotropic tide models, which improved with increased computing power and data assimilation from satellite altimetry ~~(Egbert et al. (1994); Le Provost et al. (1994); Parke a~~ ~~). However, baroclinic models have historically excluded incorporating the tides.~~ (Egbert et al., 1994; Le Provost et al., 1994; Parke and He~~r~~ . The first studies of tides in a baroclinic model were performed in ~~a regional configuration (Cummins and Oey (1997); Kang et al. (2002); M~~ ~~)~~regional configurations (Cummins and Oey, 1997; Kang et al., 2002; Merrifield et al., 2001). In the past two decades, as computers have improved, tides have been explicitly incorporated into ocean general circulation models ~~(Arbic (2022); Arbic et al. (2010); Müll~~ ~~)~~(Arbic, 2022; Arbic et al., 2010; Müller et al., 2010; Schiller and Fiedler, 2007; Thomas et al., 2001; Rocha et al., 2016; Waterhouse et al . Running such models with combined tidal and atmospheric forcing at high spatial resolution ~~allows for large scale investigations~~ enables investigation of the interactions of barotropic and internal tides with ~~smaller scale oceanic phenomena , such as~~ oceanic phenomena across a wide range of scales, including mesoscale eddies, and other components of the Earth system including the cryosphere.

An important effect to capture when modeling the tides is Self Attraction and Loading (SAL). This encompasses the physical effects of the self gravitation of the oceanic tidal elevations, the elastic response of the Earth's crust to the loading of the ocean tide, and resulting changes in the Earth's gravitational potential due to the self gravitation of the deformed solid Earth ~~(Hendershott (1972))~~(Hendershott, 1972). SAL has ~~large effects on the~~ a large effect on tides, changing ~~the~~ their amplitude by up to 20% and impacting ~~the~~ their phase significantly as well ~~(Gordeev et al. (1977))~~(Gordeev et al., 1977). A simple computationally efficient approach to computing SAL ~~in models~~ uses the so-called scalar approximation ~~(Accad and Pekeris (1978) ~~)~~(Accad and Pekeris, 1978), in which the SAL forcing term is approximated as a constant multiplied by the tidal elevation.

The scalar approximation ~~, while simple and computationally efficient, is, however , less accurate that a fuller~~ however is less accurate than a treatment using spherical harmonics, which properly account for the ~~different responses~~ response of the ocean and solid Earth to harmonics of different scales ~~(Ray (1998)).~~ (Ray, 1998). Including the spherical harmonics SAL in tide models often took an iterative approach using offline computations (Arbic et al., 2004; Egbert et al., 2004), where the SAL was calculated outside of the model run. Early attempts to use the spherical ~~harmonic SAL inlinein models, as they are running, were computationally expensive (Stepanov and Hughes (2004))~~harmonics SAL inline, as the model is running, found it to be too computationally expensive (Stepanov and Hughes, 2004). This is because SAL ~~is inherently a global calculation~~requires global communication, in contrast to other terms in the momentum equations of numerical ocean models. More recent ~~work,~~ modeling using an inline spherical harmonics SAL has been aided by improvements in computational power ~~, have still focused on the use of spherical harmonicsto compute SAL inline (Barton et al. (2022); Brus et al. (2023); Wang et al. (2024) ~~)~~(Barton et al., 2022; Brus et al., 2023; Wang et al., 2024), yet this approach still encounters limitations on accuracy around

coastlines (more below), and the fact that spherical harmonics, being global quantities, cannot easily be used in regional models.

~~In this work, we present an alternative to the spherical harmonic computation, based on the computation of a convolution with a SAL~~ Another approach to computing SAL, often used in the geodesy community, is based on convolution of the sea surface height with a Green's function (Farrell, 1972; Schrama, 2005; Agnew, 2012; Martens et al., 2019). This approach has been explored in post-processing contexts, but has never been incorporated into an ocean model due to the expense of computing the convolution integral over the sphere representing the Earth surface. Here we employ the recently developed Cubed Sphere Fast Multipole Method (CSFMM) to reduce the cost of computing the integral and enable inline SAL: calculations (Chen and Krasny, 2025) . ~~There are a number of limitations to the spherical harmonic based SAL, including limitations on accuracy and the fact that spherical harmonics, being a global quantity, cannot easily be used in regional models.~~ The convolution ~~based SAL offers an alternative that could be incorporated into regional models in the future, and that offers improvements in the accuracy of the computed SAL, as we will show later. Sec. 2 describes our convolution based SAL . Sec.~~SAL is implemented in the Modular Ocean Model, version 6, and the results show that it provides more accurate tides than those obtained with the spherical harmonics approach.

The paper is organized as follows. Section 2 presents the governing equations, describes the various methods for computing SAL, introduces our convolution SAL technique, and presents results comparing the different methods using a snapshot of the tidal sea surface height. Section 3 describes the model configuration ~~we use~~ used to test the convolution SAL~~, and Sec. 4 describes the results of our simulations, with a special emphasis on~~ . Section 4 presents results comparing tidal errors and computational ~~efficiencies~~ efficiency using the convolution and spherical ~~harmonic approaches.~~ harmonics approaches. Conclusions are presented in Section 5.

2 Methods and Implementation

The Modular Ocean Model ~~,~~ version 6 (MOM6~~, Adcroft et al. (2019)) ,~~) is a widely used open source numerical ocean general circulation model (Adcroft et al., 2019). The model is hydrostatic ~~,~~ and solves either a Boussinesq or non-Boussinesq equation set. ~~For this paper, we use the model in~~ Here we use a single layer configuration ~~, in which case the equations for the dynamics~~ in which the dynamical equations reduce to the shallow water equations ~~:~~ on a sphere,

$$\frac{\partial \boldsymbol{u}}{\partial t} + (\boldsymbol{u}\cdot\nabla)\boldsymbol{u} + \boldsymbol{f}\times\boldsymbol{u} = -g\nabla\eta + \mathcal{F}, \tag{1}$$

$$\frac{\partial \eta}{\partial t} + \nabla\cdot(h\boldsymbol{u}) = 0, \tag{2}$$

where t is time, $\boldsymbol{u}$ is the horizontal fluid velocity, $\boldsymbol{f} = f\boldsymbol{e}_r$, where f is the Coriolis parameter and $\boldsymbol{e}_r$ is the radial ~~outwards~~ outward unit vector, η is the perturbation sea surface height, g is acceleration due to gravity, $\mathcal{F}$ are other forces (for instance, friction), and h is the total water column thickness. If the ocean floor has height $b(\boldsymbol{x})$, then ~~h and η are related as~~ $\eta(t,\boldsymbol{x}) = h(t,\boldsymbol{x}) + b(\boldsymbol{x})$. ~~Eq. 1 describes~~ Equation 1 expresses the balance of momentum, and Eq. 2 ~~describes~~ expresses the conservation of mass. For multi-layer configurations, this ~~equation set~~ system can be supplemented with thermodynamic equations~~. The~~

~~equation set~~ , and in that case it is often replaced by the more general Boussinesq or non-Boussinesq equations~~in the multi-layer case~~. The horizontal grid is based on a global tripolar discretization with an Arakawa C-grid.

~~For this work , we include tidal forcing , SAL, wave drag, quadratic bottom boundary layer drag, and horizontal viscosity. Thus, our $\mathcal{F}$ takes the form~~ In this work the forcing term has several components,

$$\mathcal{F} = g\nabla(\eta_{\mathrm{EQ}} + \eta_{\mathrm{SAL}}) + \boldsymbol{F}_{\mathrm{wave}} + \boldsymbol{F}_{\mathrm{quad}} + \boldsymbol{F}_h, \tag{3}$$

where η_{EQ} ~~is the~~ represents equilibrium tidal forcing, η_{SAL} is the ~~forcing due to SAL~~ SAL potential, $\boldsymbol{F}_{\mathrm{wave}}$ is ~~parametrized~~ the linear wave drag, $\boldsymbol{F}_{\mathrm{quad}}$ is quadratic bottom boundary layer drag, and $\boldsymbol{F}_h$ is horizontal viscosity. The linear wave drag includes a ~~non-dimensional~~ tunable parameter χ. Further details on the wave drag scheme are given ~~in~~ by Jayne and St. Laurent (2001) and Buijsman et al. (2015). ~~The gradient of the SAL term has two components. We can write the SAL acceleration as~~

~~$$g\nabla\eta_{\mathrm{SAL}} = \frac{g}{R_E}\frac{\partial \eta_{\mathrm{SAL}}}{\partial \theta}\boldsymbol{e}_\theta + \frac{g}{R_E\cos\theta}\frac{\partial \eta_{\mathrm{SAL}}}{\partial \phi}\boldsymbol{e}_\phi$$~~

~~where θ is the latitude, ϕ is the longitude, $\boldsymbol{e}_\theta$ is the unit vector in the latitudinal direction, $\boldsymbol{e}_\phi$ is the unit vector in the longitudinal direction, and R_E is the radius of the Earth. The coefficient of $\boldsymbol{e}_\phi$ is then the zonal acceleration, and the coefficient of $\boldsymbol{e}_\theta$ is the meridional acceleration.~~ We refer to η_{SAL} as the SAL potential and $g\nabla\eta_{\mathrm{SAL}}$ as the SAL acceleration.

2.1 Spherical Harmonics for Computing SAL

Recent efforts ~~in computing SAL (Barton et al. (2022); Brus et al. (2023); Wang et al. (2024)) have used the spherical harmonic transform in line. If the~~ to compute SAL inline (Barton et al., 2022; Brus et al., 2023; Wang et al., 2024) have used spherical harmonics. In this technique, the spherical harmonics decomposition of the sea surface height η ~~has spherical harmonic components~~ is computed, with spherical harmonic coefficients $\widehat{\eta}_{n,m}$ ~~, then the SAL potential is given as~~ given by

$$\eta_{\mathrm{SAL}}(\theta,\phi) = \sum_{n=0}^{\infty}\sum_{m=-n}^{n}\frac{3\rho_w(1+k'_n-h'_n)}{\rho_e(2n+1)}\widehat{\eta}_{n,m} = \int_0^{2\pi}\int_0^{\pi} Y_n^m(\theta,\phi)\eta(\theta,\phi)\cos\theta d\theta d\phi, \tag{4}$$

where Y_n^m is the degree n order m spherical harmonic, ~~ρ_w is the average density of seawater in kilograms per cubic meter, ρ_e is the~~ θ is the latitude, and ϕ is the longitude. In practice two approaches are available to compute these coefficients. One approach uses a fast spherical harmonics transform (SHT) to reduce the operation count (Barton et al., 2022), but this approach faces challenges with parallel scaling, and additional interpolation steps are needed if the sea surface height is not given on a latitude-longitude grid. Another approach computes the integrals in Eq. (4) directly without using a fast transform as in Brus et al. (2023) and Wang et al. (2024). In this case the operation count is not reduced, but the direct calculation is better suited for parallelization.

Given the coefficients $\widehat{\eta}_{n,m}$, the SAL potential has the expansion

$$\eta_{\mathrm{SAL}}(\theta,\phi) = \sum_{n=0}^{\infty}\sum_{m=-n}^{n}\frac{3\rho_w(1+k'_n-h'_n)}{\rho_e(2n+1)}\widehat{\eta}_{n,m}Y_n^m(\theta,\phi), \tag{5}$$

where ρ_w and ρ_e are the average density of seawater and the Earth in kilograms per cubic meter, and k'_n and h'_n are the modified ~~Load Love Numbers~~ load Love numbers (LLNs) ~~, as discussed in Farrell (1972). Typical values we use for a single layer model configuration are a seawater density $\rho_w = 1035 kg m^{-3}$ and an Earthdensity of $\rho_e = 5517 kg m^{-3}$. When used in~~ as discussed by Farrell (1972). We use average values for the real Earth, $\rho_w = 1035\,\mathrm{kg\,m^{-3}}$, $\rho_e = 5517\,\mathrm{kg\,m^{-3}}$. When a multi-layer model is used, the sea surface height is replaced with the bottom pressure anomaly ~~, and corresponding adjustments are made to the coefficients~~and the coefficients $\widehat{\eta}_{n,m}$ are adjusted appropriately. In practice ~~, the sum~~ the sum in Eq. (5) is truncated, ~~usually~~ for example going up to ~~$n = 40$ (Brus et al. (2023)). For computing the $\widehat{\eta}_{n,m}$, two main approaches are used. The first is to employ a fast spherical harmonic transform (Barton et al. (2022)), but this faces challenges with parallel scaling. Additionally, on grids that are not latitude longitude grids, there are additional interpolation steps needed. The second is to directly compute the integrals~~

~~$$\widehat{\eta}_{n,m} = \int_0^{2\pi}\int_0^{\pi} Y_n^m(\theta,\phi)\eta(\theta,\phi)\sin\theta d\theta d\phi,$$~~

~~where Y_n^m is the degree n order m spherical harmonic (Brus et al. (2023); Wang et al. (2024)). This approach is better suited for parallelization, but can be prone to aliasing. Additionally, this spherical harmonic technique is susceptible to the Gibbs phenomenon near coastlines. The Gibbs phenomenon is a numerical effect that occurs when using Fourier series to approximate discontinuous functions. A finite truncation of the Fourier series near a discontinuity in the function being approximated will result in oscillatory errors, overshooting and undershooting the function. These errors do not decrease in magnitude as the number of Fourier components increases.~~ degree $N = 40$ (Brus et al., 2023), since using larger degrees has not significantly reduced the tidal error. The fact that tidal errors do not decrease past $N = 40$ can be attributed to Gibbs phenomenon and aliasing errors that occur when high wavenumber components in the solution are projected to low wavenumbers if the underlying spatial grid is not sufficiently fine (Sansò, 1990; Jekeli, 1996; Chen et al., 2009). These errors will be largest in coastal regions, and coastal tides have a significant back effect on the open ocean tides (Arbic et al., 2009). After computing the SAL potential η_{SAL}, the SAL acceleration $g\nabla\eta_{\mathrm{SAL}}$ is computed by finite differences, which can lead to additional errors by amplifying high wavenumber errors in η_{SAL}.

2.2 ~~The~~ Gibbs Phenomenon

The Gibbs phenomenon ~~is a type of oscillatory error that occurs when working with~~ occurs when truncating the Fourier series of a ~~function~~ periodic function f with a jump discontinuity ~~(Gottlieb and Shu (1997)). Let g be a periodic function with period L and a jump discontinuityat a point x_0 with a limit from the left of $f(x_0^-)$ and a limit from the right of $f(x_0^+)$. Then, for any finite truncation~~ (Gottlieb and Shu, 1997). If f has a jump discontinuity, then finite truncations of the Fourier series will overshoot and undershoot around the discontinuity. This overshoot has a magnitude of ~~g, at the point x_0, the Fourier series will converge to $1/2(f(x_0^-) + f(x_0^+))$, but on both sides of the jump discontinuity, there will be an overshoot of approximately 9% and a corresponding undershoot of~~ approximately 9%~~. The size of this over and undershoot does not decrease when increasing the~~

~~number of Fourier components~~ , and this oscillatory error does not diminish as more terms are used, but instead ~~the oscillatory error will become~~ it becomes sharper and more concentrated around the discontinuity.

In the context of ~~ocean modeling~~computing SAL, the Gibbs phenomenon ~~manifests in finite truncations of spherical harmonic seriesaround coastlines~~may arise from the finite truncation of a spherical harmonics series. When computing the spherical harmonic coefficients of ~~an ocean data field, such as~~ the sea surface height ~~, the value of the data field is usually set to 0~~ $\widehat{\eta}_{n,m}$, the data field η is set to zero over land. While ~~this is~~ physically reasonable, ~~it~~ this essentially introduces a jump discontinuity along coastlines, which ~~then~~ adversely affects the convergence of ~~spherical harmonic series.~~ the series. The geodesy community has known about issues with Gibbs phenomenon in spherical harmonics calculations and has advocated for an alternative based on convolution with a Green's function (Merriam, 1980; Schrama, 2005). Before examining that approach however, we consider a method for eliminating the Gibbs phenomenon.

2.2.1 ~~Cesàro Summation~~

2.3 Cesàro Summation

Cesàro summation is a ~~method for regularizing sums to improve their convergence properties , that can be used to reduce the impact of the Gibbs phenomenon.To perform Cesàro summation, we first create~~ general method for improving the convergence properties of a series. In the case of the spherical harmonics series in Eq. (4), one defines the partial sums

$$S_J = \sum_{n=0}^{J} \sum_{m=-n}^{n} \frac{3\rho_w(1+k'_n-h'_n)}{\rho_e(2n+1)} \widehat{\eta}_{n,m} Y_n^m(\theta,\phi), \tag{6}$$

~~before then averaging the partial sums~~ and then averages them to obtain the approximation

$$\eta_{\mathrm{SAL}}(\theta,\phi) \approx \frac{1}{N+1} \sum\nolimits_{n=0}^{} {}_{J=0}^{N} S_{nJ}, \tag{7}$$

which is equivalent to ~~taking the modified sum~~ modifying the coefficients of the original series,

$$\eta_{\mathrm{SAL}}(\theta,\phi) \approx \sum_{n=0}^{N} \sum_{m=-n}^{n} \left(1 - \frac{n}{N+1}\right) \frac{3\rho_w(1+k'_n-h'_n)}{\rho_e(2n+1)} \widehat{\eta}_{n,m} Y_n^m(\theta,\phi). \tag{8}$$

This technique can be implemented by modifying the existing spherical ~~harmonic~~ harmonics computation with no additional cost. ~~This modification helps to~~ The hope is that this technique will reduce the Gibbs phenomenon along coastlines, ~~but~~ however at the same time, it introduces ~~error by acting as a modification on~~ an error by effectively modifying the LLNs. As far as we know, Cesàro summation has not previously been applied in spherical harmonics SAL computations.

2.4 ~~Convolutions for Computing SAL~~

2.4 Convolution for Computing SAL

We now describe our alternative to spherical harmonics . The convolution theorem for spherical harmonics (Driscoll and Healy (1994)) states that

$$\widehat{(F*G)}_n^m = \sqrt{\frac{4\pi}{2n+1}}\widehat{F}_n^m \widehat{G}_n^0,$$

where F and G are two functions, $F*G$ is the spherical convolution of F and G, $\widehat{F}_n^m$ is the degree n order m spherical harmonic coefficient of F, and likewise for $\widehat{G}_n^0$ and $\widehat{(F*G)}_n^m$. To apply this to SAL , we will take F to be the sea surface height η and G to be an unknown Green's function for the SAL. The convolution of the sea surface height η and G_{SAL} will be the SAL potential η_{SAL}. Thus, $F*G$ will be η_{SAL}. Thus, using Eq. 5, we find that the spherical harmonic coefficients of the Green's function are It is well known that the SAL potential can be computed as a convolution on the unit sphere S,

$$\overset{0}{\eta}_{\mathrm{SAL},n} = \frac{3\rho_w(1+k'_n-h'_n)}{\rho_e\sqrt{4\pi(2n+1)}}\int_S G_{\mathrm{SAL}}(\boldsymbol{x}\cdot\boldsymbol{y})\eta(\boldsymbol{y})dS(\boldsymbol{y}), \quad \boldsymbol{x},\boldsymbol{y}\in S, \tag{9}$$

which we sum to give where the SAL Green's function as is

$$G_{\mathrm{SAL}}(\boldsymbol{x},\boldsymbol{y}) = \sum_{n=0}^{\infty}\frac{3\rho_w(1+k'_n-h'_n)}{4\pi\rho_e}P_n(\boldsymbol{x}\cdot\boldsymbol{y}), \tag{10}$$

where and P_n is the n-th Legendre polynomial and $\boldsymbol{x}$ and $\boldsymbol{y}$ are points on the sphere. With this Green's function, the SAL potential can then be computed as

$$\eta_{\mathrm{SAL}}(\boldsymbol{x}) = \int_S G_{\mathrm{SAL}}(\boldsymbol{x}\cdot\boldsymbol{y})\eta(\boldsymbol{y})dS(\boldsymbol{y}),$$

where $\boldsymbol{x}$ and $\boldsymbol{y}$ are points on the sphere, and $\gamma(\boldsymbol{x},\boldsymbol{y})$ is the great circle angle between the two points, $\arccos(\boldsymbol{x}\cdot\boldsymbol{y})$.Howeverdegree Legendre polynomial (Farrell, 1972, 1973). Given a set of grid cells covering the sphere, to actually work with the integral in Eq. (9) is computed using a numerical quadrature scheme. However, truncating the Legendre series in Eq. 9, the Green's function cannot be an infinite sum. One idea is to work with a finite truncation, but this (10) and evaluating the result at a large number of grid points is computationally intensive and not feasible in an ocean model where the SAL term is computed inline at every time step. Previous investigators have employed approximations for the LLNs (Farrell, 1972; Guo et al., 2004; Schrama, 2005; Marte outside the context of an ocean model and focusing primarily on processing data. Because of the limitations of an ocean model, we take an alternative approach to maintain a reasonable runtime. Instead, we analyze the asymptotic behavior of the LLNs. Working with the LLNs presented in Wang et al. (2012), we empirically determine that

$$k'_n \approx a_1/n, \quad h'_n \approx b_0 + b_1/n,$$

determined the following approximations,

$$k'_n \approx a_1/n, \quad h'_n \approx b_0 + b_1/n, \quad a_1 = -2.7, \quad b_0 = -6.21196, \quad b_1 = 6.1. \tag{11}$$

~~with coefficients $a_1 = -2.7$, $b_0 = -6.21196$, and $b_1 = 6.1$.Using the identities (Gradshteyn and Ryzhik (2014))~~ Then substituting in Eq. (10) and using the identities (Gradshteyn and Ryzhik, 2014),

$$\sum_{n=0}^{\infty} P_n(x) = \frac{1}{\sqrt{2(1-x)}}, \quad \sum_{n=1}^{\infty} \frac{1}{n} P_n(x) = -\ln\left(\sqrt{\frac{1-x}{2}} + \frac{1-x}{2}\right), \tag{12}$$

~~we can derive~~ a closed form approximation for the Green's function ~~as~~

~~$$G_{\mathrm{SAL}}(\boldsymbol{x},\boldsymbol{y}) \approx \frac{3\rho_w}{4\pi\rho_e}\left(\frac{1-b_0}{\sqrt{2-2\boldsymbol{x}\cdot\boldsymbol{y}}} - (a_1-b_1)\ln\left(\sqrt{\frac{1-\boldsymbol{x}\cdot\boldsymbol{y}}{2}} + \frac{1-\boldsymbol{x}\cdot\boldsymbol{y}}{2}\right)\right),$$~~

is obtained,

$$G_{\mathrm{SAL}}(\boldsymbol{x},\boldsymbol{y}) \approx \frac{3\rho_w}{4\pi\rho_e}\left(\frac{1-b_0}{\sqrt{2-2\boldsymbol{x}\cdot\boldsymbol{y}}} - (a_1-b_1)\ln\left(\sqrt{\frac{1-\boldsymbol{x}\cdot\boldsymbol{y}}{2}} + \frac{1-\boldsymbol{x}\cdot\boldsymbol{y}}{2}\right)\right). \tag{13}$$

~~However, this is not yet the final form of the Green's function. Looking at~~ From Eq. ~~3, what we need is~~ (3) we see that what is needed is the gradient of the SAL ~~. Taking the gradient , we have that~~ potential, $\nabla\eta_{\mathrm{SAL}}$. Assuming η_{SAL} has been computed, the gradient could be obtained by finite differences, but this could lead to large errors in coastal regions. Instead, taking the gradient of Eq. (9), one obtains

$$\nabla\eta_{\mathrm{SAL}}(\boldsymbol{x}) = \int_S \nabla(G_{\mathrm{SAL}}(\gamma(\boldsymbol{x},\boldsymbol{y})))\eta(\boldsymbol{y})dS(\boldsymbol{y}), \tag{14}$$

~~with the horizontal gradient falling~~ where the gradient falls on the $\boldsymbol{x}$~~variable~~ -variable of the Green's function~~in the integral. Using the chain rule ,~~ . The chain rule yields the gradient of the Green's function~~is then ,~~

$$\nabla G_{\mathrm{SAL}}(\boldsymbol{x}\cdot\boldsymbol{y}) = \frac{dg_{\mathrm{SAL}}(\gamma)}{d\cos\gamma}\frac{dG_{\mathrm{SAL}}(\cos\gamma)}{d\cos\gamma}\nabla\cos\gamma(\boldsymbol{x},\boldsymbol{y}), \tag{15}$$

where $\boldsymbol{x}\cdot\boldsymbol{y} = \cos\gamma(\boldsymbol{x},\boldsymbol{y})$ and $\gamma(\boldsymbol{x},\boldsymbol{y})$ is the great circle angle between $\boldsymbol{x}$ and $\boldsymbol{y}$. ~~Taking these derivatives , we find the integral kernel for the SAL gradient is~~ Then taking these derivatives yields

$$\nabla G_{\mathrm{SAL}}(\boldsymbol{x},\boldsymbol{y}) = \frac{3\rho_w}{4\pi\rho_e R_E\sqrt{1-x_3^2}}\begin{bmatrix} y_3(1-x_3^2) - x_3(x_1y_1+x_2y_2) \\ x_1y_2 - x_2y_1 \end{bmatrix}\left(\frac{1-b_0}{(2-2\boldsymbol{x}\cdot\boldsymbol{y})^{3/2}} - \frac{(a_1-b_1)(2\boldsymbol{x}\cdot\boldsymbol{y}+\sqrt{2-2\boldsymbol{x}\cdot\boldsymbol{y}}}{2((\boldsymbol{x}\cdot\boldsymbol{y})^2-1)}\right), \tag{16}$$

where (x_1,x_2,x_3) ~~are the Cartesian components of $\boldsymbol{x}$,~~ and (y_1,y_2,y_3) are the Cartesian ~~components of~~ coordinates of $\boldsymbol{x}$ and $\boldsymbol{y}$. ~~This is no longer a~~ Previous approaches based on Kummer's transformation yield approximate Green's functions similar to Eq. (13), but with an additional Legendre series to correct for the low wavenumber behavior. While this is computationally feasible in an offline context, summing a Legendre series up to $N = 10$ increases the runtime for evaluating the Green's function ~~as it is not symmetric in $\boldsymbol{x}$ and $\boldsymbol{y}$~~by a factor of 3, and going to $N = 40$ increases the runtime by a factor of 18. Hence we choose to work with the closed form approximate Green's function in Eq. (13) as a reasonable compromise between accuracy and efficiency for inline SAL calculations.

2.4.1 ~~Fast Summation for Accelerating Convolutions~~

2.5 Fast Summation for Accelerating Convolutions

~~To discretize~~ We employ a midpoint discretization of Eq. ~~14, we use the midpoint rule. For a set of N grid points $\{\boldsymbol{x}_i\}$, the discretized integral is approximated as~~ (14) yielding an approximation for the gradient of the SAL potential,

$$\nabla\eta_{\mathrm{SAL}}(\boldsymbol{x}_i) \approx \sum_{j=1,j\neq i}^{N\,N_0} \nabla g G_{\mathrm{SAL}}(\boldsymbol{x}_i,\boldsymbol{x}_j)\eta(\boldsymbol{x}_j)A_j, \quad i=1,\ldots,N_0, \tag{17}$$

where ~~A_j is the area associated with grid point $\boldsymbol{x}_j$. First, we note that when discretized, the sum is singular when $i=j$. To remedy this, we skip the singularity by omitting~~ N_0 is the number of grid cells used in MOM6, $\boldsymbol{x}_i$ is the midpoint of a grid cell, and A_i is the grid cell area. As the SAL acceleration is computed at cell centers, interpolation is performed to obtain values at cell edges. The kernel singularity at $i=j$ ~~from the sum. Second, we note that this sum scales like $O(N^2)$~~is skipped, which is consistent with taking the Cauchy principal value of the integral. If the sums in Eq. (17) are computed directly using loops over the indices i and j, the operation count scales like $O(N_0^2)$, which is prohibitive for ~~scaling to high resolutions. We use fast summation to avoid this issue. Fast summation refers to a family of techniques for approximating such sums in $O(N\log N)$ or $O(N)$ time complexity. For this, we use the~~ reaching high resolution. Various fast summation methods have been developed to accelerate the computation of such sums including the treecode (Barnes and Hut, 1986) and Fast Multipole Method (Greengard and Rokhlin, 1987).

Here we employ the recently developed Cubed Sphere Fast Multipole Method (CSFMM) ~~presented in Chen and Krasny (2025)~~ to reduce the operation count to $O(N_0)$ (Chen and Krasny, 2025). The CSFMM ~~is based on the use of~~ applies barycentric Lagrange interpolation to approximate the kernel (Berrut and Trefethen, 2004), with proxy points defined by ~~the tensor product~~ a tensor product grid of Chebyshev points in a quadtree of cubed sphere grid cells. The scheme introduces an error whose amplitude is controlled by two user-specified parameters, the interpolation degree n_0 and a parameter θ_0 controlling the size and separation of the cubed sphere ~~tree structure, allows for the computation of the discretized integral in $O(N)$ computation. The cubed sphere tree structure is used to divide points into clusters, and when a cluster has many points, barycentric Lagrange interpolation is then used to perform approximations to reduce the amount of computation. This introduces a small and controllable amount of error. The use of the tree structure~~ grid cells. In contrast to spherical harmonics approximations, the interpolation is local, and this approach does not encounter the Gibbs phenomenon. In addition, the quadtree structure of the cubed sphere grid cells naturally adapts to the irregular distribution of ocean grid points around coastlines~~, and this method additionally operates entirely on the sphere andnot in 3d Cartesian space, as with many other methods.~~. A detailed discussion of the error behavior of spherical convolutions and the CSFMM is presented in Chen and Krasny (2025).

3 ~~Simulation Details~~

2.1 Comparison of Methods

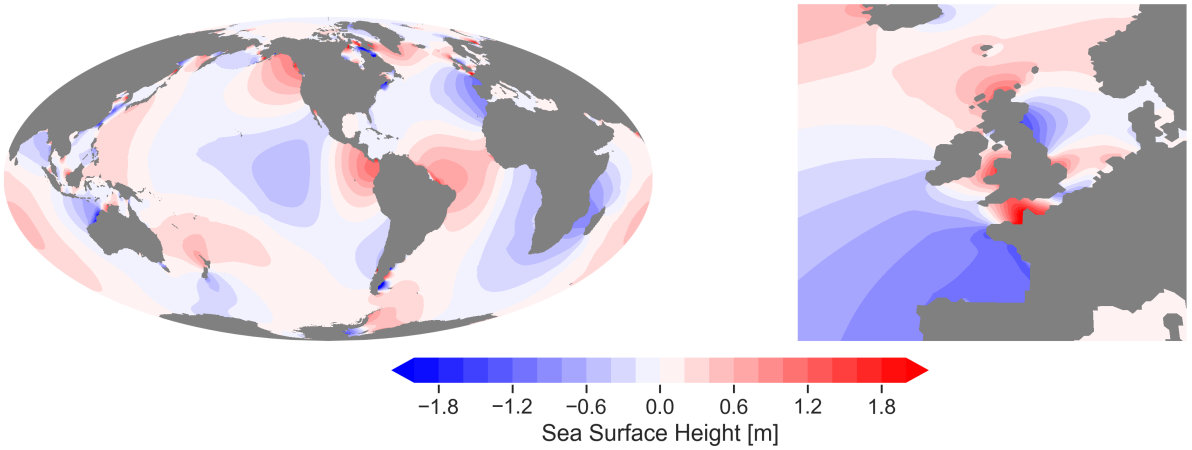

Figure 1. Global snapshot of tidal sea surface height used to compare different SAL computation methods. The right panel is a zoomed version of the left panel focusing on the Northeast Atlantic, a region of exceptionally large coastal tides. The SSH snapshot is on a MOM6 grid with 0.08° nominal grid spacing, taken from an existing MOM6 barotropic tidal simulation.

~~We implement this convolution~~ Before discussing the implementation of convolution SAL in MOM6, we compare the various methods for computing SAL without any confounding factors the model may introduce. We compute the SAL acceleration on a MOM6 grid with 0.08° nominal grid spacing for the global snapshot of tidal sea surface height (SSH) shown in Fig. 1 using the various methods described in the previous sections. The SSH snapshot comes from a tidal MOM6 run, with SAL computed using the SHT with $N = 40$. For future reference, note that the SSH in Fig. 1 apparently has discontinuities along certain coastlines. In the following tests, the SHT is used with maximum degree $N = 40$ and $N = 200$, and the Cesàro SHT is used with $N = 40$, $N = 200$, and $N = 400$. These are compared with the convolution approach, which uses CSFMM parameters $n_0 = 2$ and ~~CSFMM in MOM6. To evaluate the~~ $\theta_0 = 0.9$. Global zonal and meridional accelerations are plotted in Figs. 2 and 3, and accelerations focused on the Northeast Atlantic are plotted in Figs. 4 and 5. Figure 6 plots the spectral density of the zonal acceleration in Fig. 2. As all the calculations are based on the same reference SSH snapshot, differences can be attributed to the different methods of computing SAL, as opposed to confounding factors from the other (non-SAL) factors in the model, such as wave drag, bathymetry, and so on.

Looking first at the global zonal and meridional accelerations, there is general agreement among all the results. As the maximum degree increases from $N = 40$ to $N = 200$ in the SHT computation, one observes less large scale waviness in the contour lines, due to a reduction in truncation error. While differences between the $N = 40$ and $N = 200$ results may appear large, they are actually quite small, less than $10^{-8}\mathrm{m\,s^{-2}}$ in the open ocean. Additionally, the large scale patterns of the Cesàro SHT result broadly match the unmodified SHT result, with small differences. This is because Cesàro summation has the largest effect on small scales at high wavenumber, while the plots mainly depict the low wavenumber large scale structure. Lastly, there are some differences in the large scale structure between the convolution result and the five SHT computations. This is

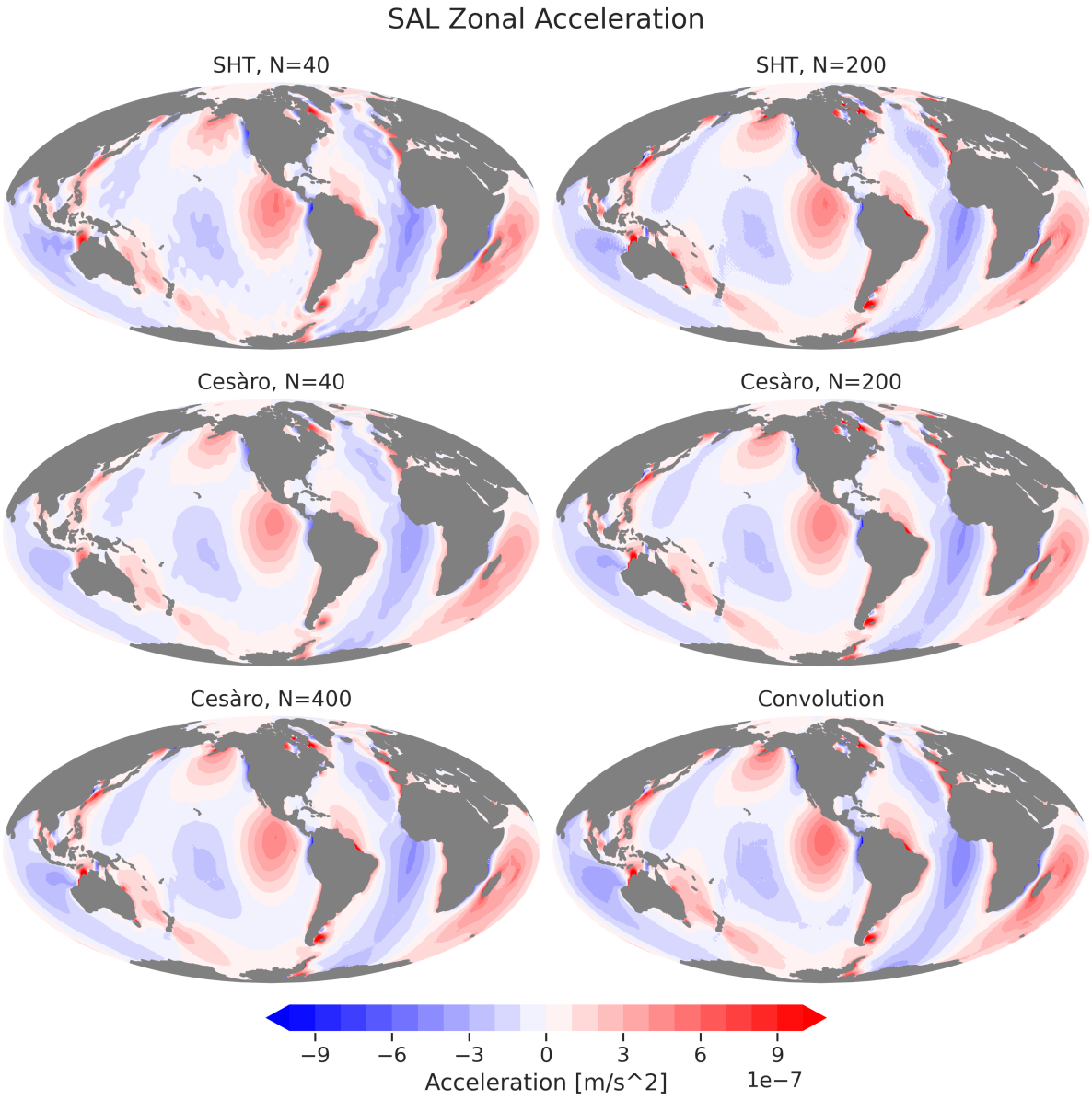

Figure 2. SAL zonal acceleration for the tidal sea surface height snapshot in Fig. 1, computed using spherical harmonics transform (SHT) with $N = 40$, $N = 200$, Cesàro regularized SHT with $N = 40$, $N = 200$, $N = 400$, and convolution.

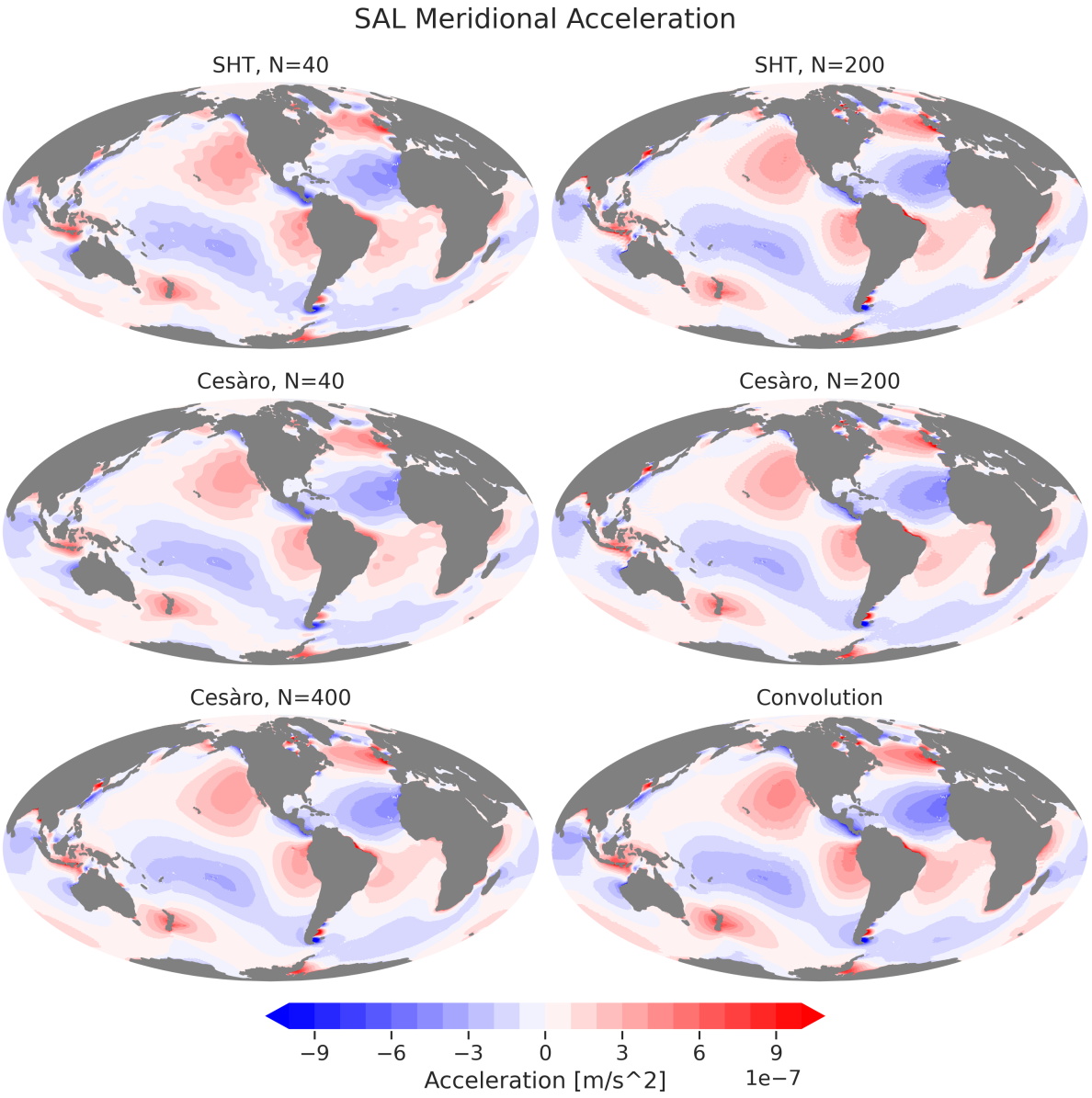

Figure 3. SAL meridional acceleration for the sea surface height snapshot in Fig. 1, computed using spherical harmonics transform (SHT) with $N = 40$, $N = 200$, Cesàro regularized SHT with $N = 40$, $N = 200$, $N = 400$, and convolution.

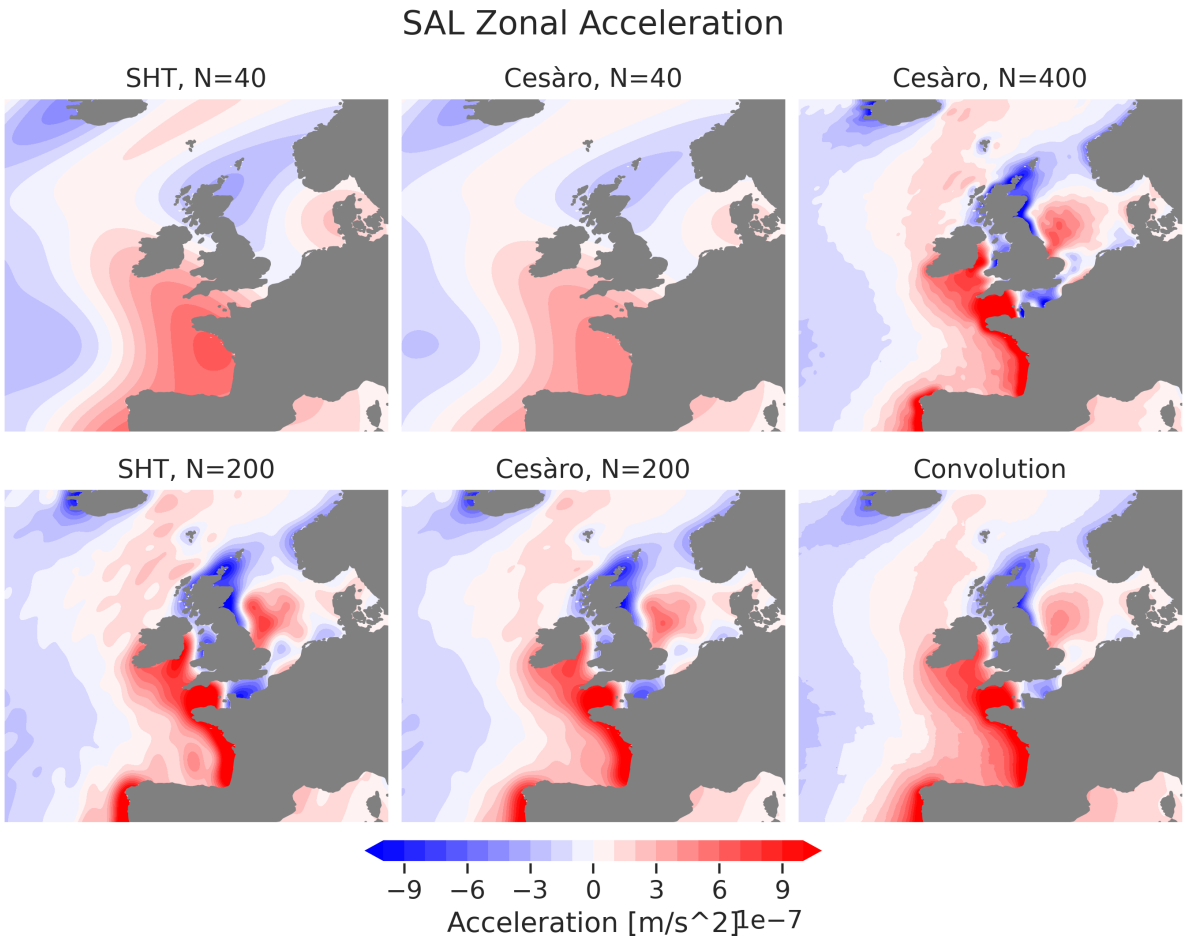

Figure 4. As in Fig. 2, focusing on the Northeast Atlantic.

because the LLN approximations used in deriving the closed form SAL Green's function are least accurate at low wavenumber and have the greatest impact at large scales.

Next consider the regional accelerations in Figs. 4 and 5. Clear differences can be seen between the SHT results with $N = 40$ and $N = 200$, where $N = 200$ resolves small scale features in coastal regions while predicting larger coastal amplitudes. As coastal regions are spanned by relatively few grid cells, aliasing of high degree spherical harmonics may contribute to these large amplitudes. Comparing the $N = 40$ SHT result with the $N = 40$ Cesàro SHT result, one sees the regularization effect of the latter as maximum amplitudes are smaller. At $N = 200$, the Cesàro sum resolves most of the small scale structure of the unmodified SHT, but there is less waviness in the contour lines and the maximum amplitudes are smaller. The $N = 400$ Cesàro result further reduces the waviness and resolves small scale features, but also increases the coastal amplitudes. The convolution result is similar to the high degree SHT results, but it predicts smaller coastal amplitudes. The LLN approximations

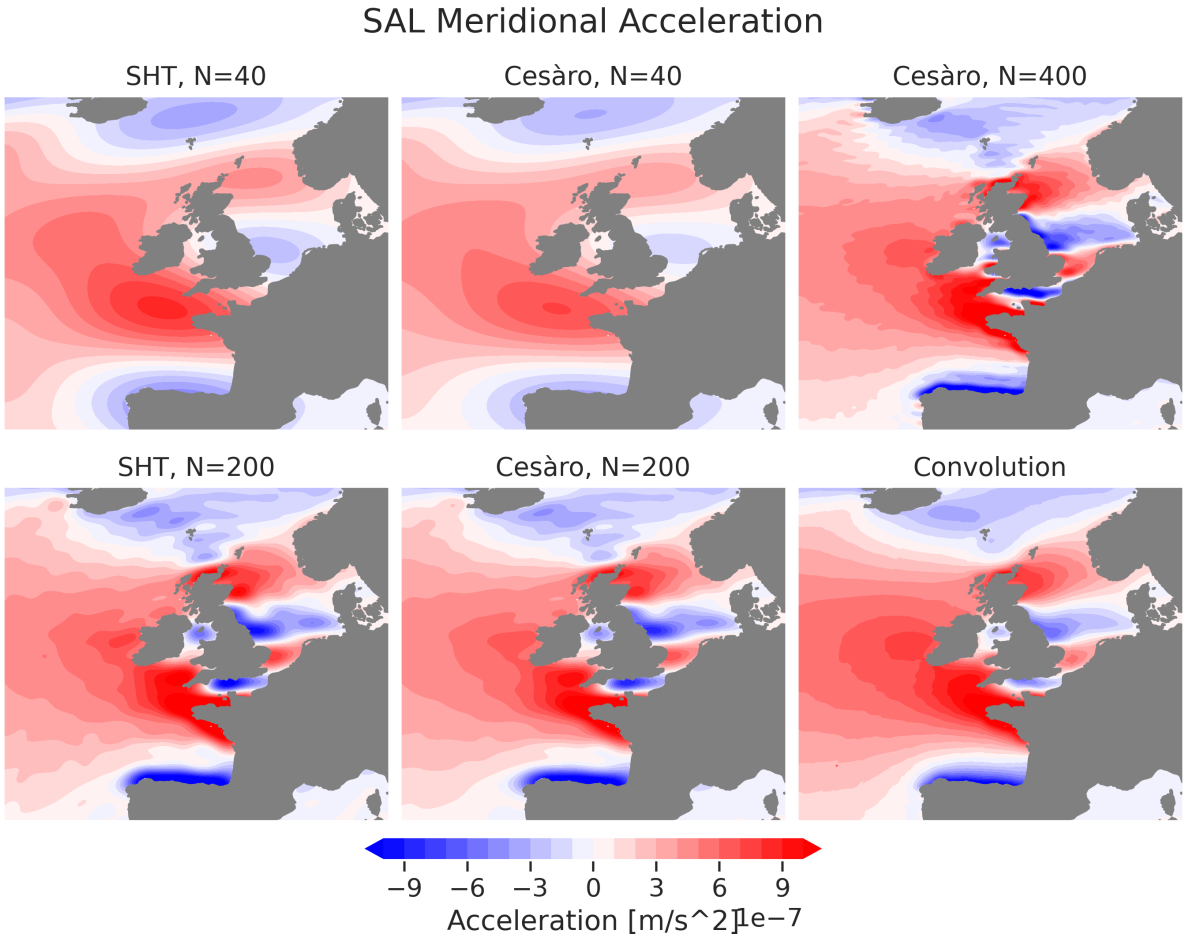

Figure 5. As in Fig. 3, focusing on the Northeast Atlantic.

used in deriving the closed form SAL Green's function are most accurate at high wavenumber and small scales. While the convolution approach has errors in the approximation SAL Green's function, quadrature error in computing the integral, and interpolation error from the CSFMM, it avoids the Gibbs phenomenon, aliasing error, and finite difference errors present in the SHT calculations.

To gain further insight into the methods, Fig. 6 shows the normalized spectral density of the SAL zonal acceleration. There is general agreement among the five SHT results, which decay roughly as $O(N^{-1})$. Comparing the $N = 40$ SHT with the $N = 40$ Cesàro SHT, the latter spectrum falls off slightly faster at high wavenumber. A similar trend is seen at $N = 200$, but to a lesser degree. In contrast, the convolution spectrum falls off significantly faster at high wavenumber, decaying like $O(N^{-2})$, which is consistent with the smoother acceleration fields seen in Fig. 4 and Fig. 5.

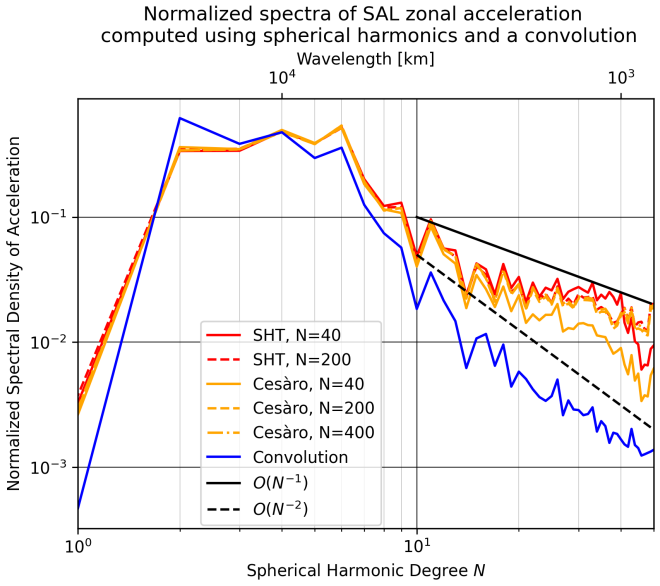

Figure 6. Normalized spectral density of the global SAL zonal acceleration field shown in Fig. 2. A spherical harmonic of degree N has wavelength $2\pi R_E/N$.

3 Simulation Details

The convolution~~method for computing SAL , we run MOM6 and force the model with the~~ /CSFMM technique described above was implemented in MOM6. The model is run with zero initial velocity and M_2 ~~tide. The model is initialized with zero velocity initial conditions, and is run~~ tidal forcing for 20 days with ~~a time step of $\Delta t = 180\,s$. The~~ time step $\Delta t = 180\,\mathrm{s}$. The SAL acceleration is computed inline at every time step and the last three days of ~~model~~ output are used ~~for the error computation. We test~~ to evaluate the results. A single level configuration is used with two different ~~grid spacings:~~ grids, one with nominal spacing $0.36°$ (typical of ~~0.36 degrees (a grid spacing typical of~~ long duration low-resolution climate ~~change~~ simulations), and one with nominal spacing ~~of 0.08 degrees (a grid spacing typical for higher-resolution simulationsusually run over shorter durations than climate change simulations). We use a single level configuration. The SAL term is computed at every time step. The~~ $0.08°$ (typical of short duration high-resolution simulations). The model was run on ~~Derecho (Computational and Information Systems Laboratory). We use a~~ the Derecho computer system at NCAR (Computational and Information Systems Laboratory, 2023). The topography and wave drag are based on GEBCO 2023. ~~For both grids, we use several different SAL configurations . We use the spherical harmonic SAL with $n = 40$ spherical harmonic components, a commonly used configuration, as well as $n = 200$ spherical harmonic components, to test the convergence. We also test the~~ Several configurations are tested: SHT with $N = 40, 200,$ Cesàro ~~modified spherical harmonic SAL with $n = 40$, $n = 200$, and $n = 400$ spherical harmonic components. Lastly, we test the convolutionSAL as well.~~ SHT with $N = 40, 200, 400,$ and convolution.

3.0.1 ~~Measuring Error~~

3.1 Measuring Error

To measure the error in the model tides, ~~we compare~~ the model output is compared with the TPXO9 dataset ~~(Erofeeva and Egbert (2018))~~(Erofeeva and Egbert, 2018), which comes from a hydrodynamical model that assimilates satellite observations of tidal sea surface heights. ~~To do this, we~~ We first compute

$$D^2 = \frac{1}{2}(A^2_{\mathrm{TPXO}} - A^2_{\mathrm{MOM6}}) - A_{\mathrm{TPXO}} A_{\mathrm{MOM6}} \cos(\varphi_{\mathrm{TPXO}} - \varphi_{\mathrm{MOM6}}), \tag{18}$$

at each grid point, where A is the amplitude of the tidal constituent and φ is the Greenwich phase lag. The ~~error is then computed as~~ root mean square error (RMSE) is then defined as

$$\mathrm{RMSE} = \left(\frac{1}{4\pi R_E^2} \int_S D^2 dS \right)^{1/2} . \tag{19}$$

~~We can also decompose the RMSE~~ The RMSE can be decomposed into an amplitude error and a phase error~~. Additionally, we compute the error for both~~ (Shriver et al., 2012). The RMSE is also computed for two different domains: over the entire ocean, and ~~for the grid points between 66 degrees south and 66 degrees~~ over grid points lying between 66° south and 66° north that have a depth of greater than 1000 meters~~in order to filter out the impact from coastal topography and limited satellite altimetry coverage in polar areas~~. The latter computation removes coastal regions and polar regions, where data-assimilative tide models such as TPXO are less accurate (Stammer et al., 2014).

3.1.1 ~~Tuning~~

3.2 Tuning

The parameter χ in the wave drag scheme is tuned for each method of computing ~~the SAL . The tuning is performed~~ SAL in order to minimize the ~~$RMSE$, but one~~ RMSE. One can understand the need for tuning using energy arguments ~~(Arbic et al. (2004)). If~~ (Arbic et al., 2004); if χ is too large, then too much energy ~~will be~~ is dissipated, and conversely if χ is ~~not large enough~~too small, then not enough energy ~~will be~~ is dissipated. Both extremes ~~above will~~ adversely affect the accuracy of the modeled tides. The different ~~ways of computing the SAL will result in~~ methods of computing SAL yield accelerations of different ~~magnitudes, and as a result,~~ amplitude and χ must change accordingly. The χ parameters ~~that are used~~ used here are presented in Table 1 and Table 2. Because of differences in how the wave drag was precomputed, the ~~wave drag coefficients~~ coefficient χ ~~at 0.36 and 0.08 degree grid spacingare of different orders of magnitude~~has a different order of magnitude at 0.36° and 0.08° grid spacing.

4 Results

4.1 TPXO9 Comparison

~~We present our error results~~ Error results are presented in Table 1 ~~and 2~~with 0.36° nominal grid spacing and in Table 2 with 0.08° nominal grid spacing. Denoting the maximum degree of spherical harmonics used as ~~n, we compare the spherical harmonic SAL with a~~ N, the SHT is compared with the Cesàro ~~modified spherical harmonic SAL~~SHT, as well as the convolution~~SAL. On a mesh with 0.36 degree~~. With 0.36° nominal grid spacing, the ~~spherical harmonic SAL with $n = 40$ results in~~ $N = 40$ SHT has a deep non-polar RMSE of 6.50 cm, with the phase error contributing 5.70 cm~~of this error~~. The global RMSE of 8.65 cm is similarly dominated by the phase error of 7.31 cm. ~~The spherical harmonic SAL run with $n = 200$ has a similar RMSE of 6.45 cm in the deep non-polar ocean and 8.54 cm in the entire ocean. With the~~ Using $N = 200$ yields only an error reduction of approximately 1%. The Cesàro ~~modified spherical harmonic SAL runs, we observe larger errors than when the standard spherical harmonic SAL is used. However, as we increase the number of spherical harmonic components used for the Cesàro spherical harmonic SAL, we observe a reduction in the error as we go from $n = 40$~~ SHT errors decrease from $N = 40$ to ~~$n = 200$~~ $N = 200$ and ~~$n = 400$. With the convolution SAL computation, we reduce the RMSE considerably from 6.50 cm to 4.10 cm, with most of the improvement coming from a reduction in~~ $N = 400$, yet even for $N = 400$ they remain larger than the $N = 40$ SHT errors. The convolution errors are smaller than the SHT errors in all cases, with the greatest reduction coming from the phase error~~, from 5.70 cm to 3.01 cm. Likewise, in the global ocean, we reduce the phase error from 7.31 cm to 4.80 cm. With the runs at 0.08 degree~~. With 0.08° nominal grid spacing, ~~we observe a significant reduction in error compared to the model runs at 0.36 degree nominal grid spacing. However, there are differences in the error behavior. First, using up to $n = 200$ degree spherical harmonics increases the error slightly, compared to using only up to $n = 40$. Additionally, in contrast to the results with 0.36 degree nominal grid spacing, in the higher resolution 0.08 degree grid spacing results,~~ significant error reduction is achieved in all cases. The $N = 200$ SHT errors are the ~~convolution SAL does not present as large of an error improvement compared to the spherical harmonic SAL.~~ smallest among the five SHT test cases. The amplitude errors are slightly larger for the convolution than for the $N = 200$ SHT, but this is compensated by smaller phase errors, so that the convolution has the smallest RMSE.

		Deep non-polar ocean			Global ocean		
0.36° nominal grid spacing	Wave drag χ	RMSE	Amplitude error	Phase error	RMSE	Amplitude error	Phase error
Spherical harmonic SAL, $N = 40$	0.8	6.50	3.18	5.70	8.65	4.63	7.31
Spherical harmonic SAL, $N = 200$	0.8	6.45	3.09	5.66	8.54	4.61	7.18
Cesàro SH SAL, $N = 40$	0.8	8.10	3.56	7.27	10.26	5.01	8.95
Cesàro SH SAL, $N = 200$	0.8	6.76	3.17	5.98	8.86	4.68	7.52
Cesàro SH SAL, $N = 400$	0.8	6.60	3.13	5.81	8.69	4.65	7.35
Convolution SAL	0.7	4.10	2.78	3.01	6.53	4.43	4.80

Table 1. Wave drag tuning parameter χ and errors for different methods of computing SAL ~~for 0.36 degree~~ with 0.36° nominal grid spacing.

		Deep non-polar ocean			Global ocean		
0.08° nominal grid spacing	Wave drag χ	RMSE	Amplitude error	Phase error	RMSE	Amplitude error	Phase error
Spherical harmonic SAL, $N = 40$	8.0	2.71	1.59	2.20	5.32	3.54	3.96
Spherical harmonic SAL, $N = 200$	8.0	2.67	1.55	2.17	5.22	3.53	3.84
Cesàro SH SAL, $N = 40$	8.0	4.50	2.34	3.85	6.78	3.98	5.49
Cesàro SH SAL, $N = 200$	8.0	3.01	1.68	2.49	5.48	3.61	4.13
Cesàro SH SAL, $N = 400$	8.0	2.84	1.61	2.33	5.35	3.57	3.98
Convolution SAL	8.2	2.36	1.70	1.63	5.06	3.64	3.52

Table 2. As in Table 1, but with ~~0.08 degree~~ 0.08° nominal grid spacing.

~~SAL acceleration computed from spherical harmonic and convolution based SAL techniques at 0.36 degree nominal grid spacing. This is at a single time step.~~

~~As in Fig. ??, but focused on the Northeast Atlantic and North Sea.~~

~~Spherical harmonic spectra of the SAL acceleration, computed from the zonal accelerations in Fig. ?? over the ocean grid points. The spectra are normalized to unit norm. The wavelength for a given spherical harmonic degree is $2\pi R_E/n$. The spectra are computed for the acceleration at a single time step.~~

4.2 Discussion

~~The question arises: what is the reason for the improvement in the results that use a convolution SAL, especially the improvement in the tidal phase? To address this, we examine the corresponding SAL acceleration, $g\nabla\eta_{\rm SAL}$, focusing on the spherical harmonic and convolution based SAL fields. The zonal and meridional acceleration for the spherical harmonic and convolution accelerations at a single time step display significant differences (~~The question arises–why are the SHT errors only slightly smaller for $N = 200$ than for $N = 40$? Figure 2 and Fig. ??~~). The overall structure of the acceleration is the same in the spherical harmonic and convolution computations. However, the spherical harmonic computation with degree $n = 40$ exhibits a large number of small oscillations, arising from the truncation of the spherical harmonic series. The spherical harmonic computation with degree $n = 200$ has a similar structure as the computation with $n = 40$,~~ 3 show that the $N = 40$ SHT results have small amplitude oscillations in the open ocean, while the $N = 200$ SHT results have similar structure but without the oscillations. ~~However, with $n = 200$, the error has not significantly reduced, so these small oscillations in the open ocean cannot explain the differences in the error between $n = 40$ and $n = 200$ simulations.There are large spurious coastal accelerations in both spherical harmonic calculations, as a result of the Gibbs phenomenon. In contrast, with the convolution based SAL, the large spurious coastal accelerations are removed.~~

~~This removal of the Gibbs phenomenonis especially apparent in zoomed-in views of coastal regions (~~The more significant difference is seen in Fig. 4 and Fig. 5, where $N = 200$ yields larger coastal accelerations than $N = 40$. Some of these large coastal accelerations are spurious overshoots due to Gibbs phenomenon, aliasing error, and finite differencing error. Similar considerations apply to the $N = 200$ and $N = 400$ Cesàro SHT results. Cesàro summation mitigates any impact of Gibbs

phenomenon, but it does nothing to remedy errors due to aliasing and finite differencing, and as a result, it also results in large coastal accelerations. By contrast as seen in Fig. ??). Using the Northeast Atlantic and North Sea regions as examples, we see a significant difference in the spatial structure of the acceleration when we go from $n = 40$ to $n = 200$ spherical harmonic components.In contrast, with the convolution 4 and Fig. 5, the convolution predicts smaller coastal accelerations, which we attribute to the absence of Gibbs phenomenon, aliasing error, we have a similar spatial structure to the spherical harmonic computation with $n = 200$, showing that we resolve fine scales, but the amplitude of the acceleration is smaller, as we have removed the Gibbs errors. The adverse impact of the Gibbs phenomenonalso explains why using $n = 200$ spherical harmonics instead of $n = 40$ spherical harmonics has a minimal impact on the tidal errors. Increasing the number of spherical harmonics used does not decrease the magnitude of the Gibbs errornear the coastlines. Instead, with more spherical harmonics, the oscillations become more concentrated along the coastlines, and when the gradient is taken with $n = 200$, the accelerations are also larger. and finite differencing error.

Another question arises–why does the removal of the Gibbs Gibbs phenomenon and aliasing error in coastal regions yield an improvement in the error observed reduce the error in the deep , non-polar ocean? We speculate that the reason for the global improvement in the tides is due to the "back effect " of regions of back effect of large resonant coastal tides upon open-ocean tides (Arbic et al. (2007, 2009); Arbic and Garrett (2010)). Changes to the tides in small coastal regions, especially those regions with large resonant coastal tides, can have a large back effect on the global tides. Thus , (Arbic et al., 2007, 2009; Arbic and Garrett, 2010) . Thus it appears that the improvements to the SAL in coastal regions as a result of using the convolution SAL can drive improvements in to the tides in the entire ocean. Further mechanistic exploration into the role of the back effect in the results shown here these calculations, as well as other potential reasons for the improvement, is left as a topic for future work.

The wavenumber spectra of the acceleration (Fig. 6) also reveals illuminating differences. While the spherical harmonic and convolution SAL have similar accelerations at low wavenumbers, at higher wave numbers, the spectra for the convolution SAL acceleration drops off much faster than it does for the spherical harmonic SAL acceleration. As a result, we can say that the convolution SAL produces a smoother acceleration. The convolution based SAL is smoother than the spherical harmonic SAL for two reasons. First, the convolutionbased SALdoes not suffer from Gibbs errors near the coastlines. In setting the sea surface height η to 0 over land, discontinuities are introduced, and any finite truncation of the spherical harmonics will have Gibbs errors. In contrast, the convolution incorporates behavior at all wavenumbers and thus, avoids finite truncation problems. Secondly, MOM6 uses a staggered C-grid. The spherical harmonic SAL computes the SAL potential at cell centers, and then uses finite differences to compute the accelerations at the cell edges. In contrast, the convolution SAL computes the SAL acceleration at the cell center, and then averages to compute the acceleration at the cell edges. The finite difference amplifies small scales, while the averaging serves to smooth them.

4.3 Runtime Performance

Strong scaling of the two methods of computing SAL at 0.36 degree nominal grid spacing.

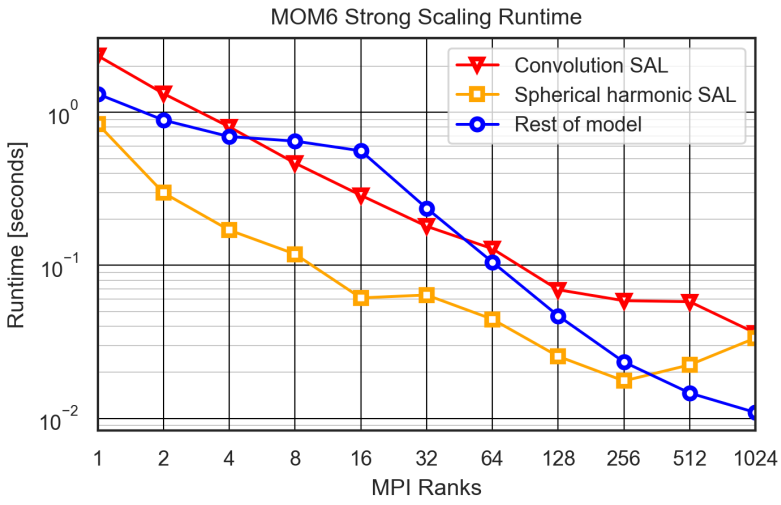

Figure 7. Single time step runtime (seconds) versus number of MPI ranks, MOM6 running with 0.36° nominal grid spacing, yielding $N_0 = 784000$ grid cells, results shown for convolution SAL, $N = 40$ spherical harmonics SAL, non-SAL portion of the calculation.

4.3 Parallel Efficiency and Runtime

~~We perform a strong scaling analysis to verify that the convolutionbased SAL computation does not have an excessive runtime impact. Using~~ A strong scaling analysis is performed to examine the parallel efficiency and runtime of the convolution/CSFMM SAL. Figure 7 shows the single time step runtime (seconds) versus the number of MPI ranks for MOM6 ~~'s internal performance analysis tools, we record the time needed for a single time step while varying the number of MPI ranks from~~ running with 0.36° nominal grid spacing yielding $N_0 = 784000$ grid cells. The runtime is shown for the convolution/CSFMM SAL, $N = 40$ spherical harmonics SAL, and non-SAL portion of the calculation. The data was collected using the internal performance analysis tools in MOM6. The SHT and convolution/CSFMM are different algorithms with different operation counts and communication patterns, and this affects their parallel efficiency. From 1 to ~~1024. The single time step runtime is displayed in Fig. 7. While the spherical harmonic computation is less expensive, it does not parallelize as well as the convolution computation, and at 1024 MPI ranks, the two methods have a similar runtime impact . The runtime impact from this SAL calculation is on the order of 1 or 2 model levels. While this impact is considerable for a single layer simulation, for a~~ 16 ranks, the SHT scales better and is faster than the convolution/CSFMM, but from 16 to 1024 ranks the convolution/CSFMM scales better than the SHT. The SHT runtime increases at 512 and 1024 ranks, presumably due to communication costs, while the convolution/CSFMM continues scaling well. In this single layer simulation the convolution/CSFMM runtime is comparable to or smaller than the non-SAL portion of the calculation, and its impact in a multi-layer simulation ~~, the runtime impact will be correspondingly~~ will be much smaller.

5 Conclusions

~~Tides are an important component of the Earth system.~~ In the numerical modeling of ocean tides, capturing the effects of SAL is ~~important for accurate simulations. Many ocean tide~~ necessary for accurate prediction of tidal amplitude and phase. Many current models employ spherical harmonics to compute ~~SAL. In this work , we present an alternative method of computing SAL , based on a spherical convolution which we accelerate with a fast multipole method. We implemented this computation in the ocean model MOM6 and ran a number of tidal simulations to validate the computation, comparing the results with the~~ the SAL acceleration. This work presents an alternative where the SAL acceleration is computed by convolving the sea surface height with an approximate Green's function. The convolution integral is discretized on a set of grid cells covering the sphere and the sums are accelerated by the Cubed Sphere Fast Multipole Method. The convolution/CSFMM was implemented in the MOM6 ocean model and compared with the default SHT as well as a Cesàro modified SHT. Errors in tidal amplitude and phase were tabulated using the TPXO9 tidal atlas ~~. The tidal error results compare favorably to results employing the spherical harmonic SAL that is currently used, and the runtime impact~~ as the reference. In these tests the convolution has smaller RMSE than the SHT. The larger SHT error is attributed to overshoots in coastal amplitude due to Gibbs phenomenon, aliasing error due to finite grid resolution, and finite difference error in computing the gradient of the SAL potential. In contrast to the global nature of spherical harmonics, the convolution/CSFMM uses local grid cell approximations which do not exhibit these errors. Parallel scaling results up to 1024 MPI ranks show that the runtime of the convolution/CSFMM is not prohibitive.

~~In this work , we~~ This work focused on global ocean models~~. However, regional ocean models are also of great importance, and incorporating the~~ , but incorporating tides and SAL in regional ~~ocean~~ models is also ~~a topic of interest (Irazoqui Apecechea et al. (2017)). Spherical harmonic SAL based techniques cannot be used in such regional models due to the inherently global nature of spherical harmonics . In the future, we plan on exploring the use of the convolution~~of interest (Irazoqui Apecechea et al., 2017) . Spherical harmonics are poorly suited for that case, and in future work we plan to explore the convolution/CSFMM SAL in regional models.

~~Additionally, there remains work to be done in the physical~~ We also envision improving the accuracy of the ~~computed SAL. The approximations used in the derivation of this SAL~~ closed form Green's function ~~introduce some error.Furthermore, there are physical effects which are not yet incorporated. In particular, the interior of the Earth is not homogeneous (Pagiatakis (1990); Scherneck).This effect is difficult to incorporate with spherical harmonics. However, a spatially varying~~ in Eq. (16) by utilizing more accurate approximations of the load Love numbers (Farrell, 1972; Guo et al., 2004; Schrama, 2005; Martens et al., 2019). Similarly, the present work employed a simple discretization of the convolution integral Eq.(17) and more accurate schemes could be considered (Agnew, 2012). Finally, an integral equation method could bypass the load Love numbers and directly compute the SAL Green's function ~~could incorporate the Earth's interior inhomogeneity~~on a grid given a model of the Earth interior. Such an approach could possibly also incorporate the inhomogeneity of the Earth interior (Pagiatakis, 1990; Scherneck, 1991).

Code and data availability. The current version of MOM6 is available from https://github.com/noaa-gfdl/MOM6 under the GNU Lesser General Public License. The exact version of the model used to produce the results used in this paper is archived on repository under DOI 10.5281/zenodo.18445619 (Chen and Wang, 2026), as are input data and scripts to run the model and produce the plots for all the simulations presented in this paper.

Author contributions. BKA and RK conceptualized the project. AC conducted the formal analysis and investigation. AC and HW produced the software. HW provided datasets. BKA and RK supervised the project. AC visualized the results and prepared the original draft. AC, HW, BKA, and RK assisted in reviewing and editing the manuscript.

Competing interests. The authors declare that they have no conflict of interest.

Acknowledgements. AC ~~is~~ was supported by the National Science Foundation Graduate Research Fellowship Program under Grant Number DGE 2241144. Any opinions, findings, and conclusions or recommendations expressed in this material are those of the authors and do not necessarily reflect the views of the National Science Foundation. BKA is grateful for sabbatical support from the Australian National University, especially Callum Shakespeare, Andy Hogg, and Adele Morrison, during the 2024–2025 academic year. BKA acknowledges support from Office of Naval Research grant N00017-22-1-2576. The authors thank Robert Hallberg (National Oceanic and Atmospheric Administration, Geophysical Fluid Dynamics Laboratory) and Alan Wallcraft (Florida State University) for useful discussions. The authors also thank Oliver Jahn (MIT, Program in Atmospheres, Oceans, and Climate) for noticing ~~a mistake~~ mistakes in the original ~~statement of Equation~~ statements of Equations 15 and 16, which ~~has~~ have since been rectified. The authors additionally thank the reviewers for helpful comments.

References

Accad, Y. and Pekeris, C. L.: Solution of the tidal equations for the M2 and S2 tides in the world oceans from a knowledge of the tidal potential alone, Philos. Trans. R. Soc. London, Ser. A, 290, 235–266, 1978.

Adcroft, A., Anderson, W., Balaji, V., Blanton, C., Bushuk, M., Dufour, C. O., Dunne, J. P., Griffies, S. M., Hallberg, R., Harrison, M. J., et al.: The GFDL global ocean and sea ice model OM4. 0: Model description and simulation features, J. Adv. Model. Earth Syst., 11, 3167–3211, 2019.

Agnew, D. C.: SPOTL: Some programs for ocean-tide loading, 2012.

Arbic, B. K.: Incorporating tides and internal gravity waves within global ocean general circulation models: A review, Prog. Oceanogr., 206, 102 824, 2022.

Arbic, B. K. and Garrett, C.: A coupled oscillator model of shelf and ocean tides, Cont. Shelf Res., 30, 564–574, 2010.

Arbic, B. K., Garner, S. T., Hallberg, R. W., and Simmons, H. L.: The accuracy of surface elevations in forward global barotropic and baroclinic tide models, Deep Sea Res. Part II, 51, 3069–3101, 2004.

Arbic, B. K., St-Laurent, P., Sutherland, G., and Garrett, C.: On the resonance and influence of the tides in Ungava Bay and Hudson Strait, Geophys. Res. Lett., 34, 2007.

Arbic, B. K., Karsten, R. H., and Garrett, C.: On tidal resonance in the global ocean and the back-effect of coastal tides upon open-ocean tides, Atmos. Ocean, 47, 239–266, 2009.

Arbic, B. K., Wallcraft, A. J., and Metzger, E. J.: Concurrent simulation of the eddying general circulation and tides in a global ocean model, Ocean Modell., 32, 175–187, 2010.

Barnes, J. and Hut, P.: A hierarchical O(NlogN) force-calculation algorithm, Nature, 324, 446–449, 1986.

Barton, K. N., Pal, N., Brus, S. R., Petersen, M. R., Arbic, B. K., Engwirda, D., Roberts, A. F., Westerink, J. J., Wirasaet, D., and Schindelegger, M.: Global barotropic tide modeling using inline self-attraction and loading in MPAS-Ocean, J. Adv. Model. Earth Syst., 14, e2022MS003 207, 2022.

Berrut, J.-P. and Trefethen, L. N.: Barycentric Lagrange interpolation, SIAM Review, 46, 501–517, 2004.

Brus, S. R., Barton, K. N., Pal, N., Roberts, A. F., Engwirda, D., Petersen, M. R., Arbic, B. K., Wirasaet, D., Westerink, J. J., and Schindelegger, M.: Scalable self attraction and loading calculations for unstructured ocean tide models, Ocean Modell., 182, 102 160, 2023.

Buijsman, M. C., Arbic, B. K., Green, J., Helber, R. W., Richman, J. G., Shriver, J. F., Timko, P., and Wallcraft, A.: Optimizing internal wave drag in a forward barotropic model with semidiurnal tides, Ocean Modell., 85, 42–55, 2015.

Chen, A. and Krasny, R.: A Cubed Sphere Fast Multipole Method, arXiv preprint arXiv:2508.13550, 2025.

Chen, A. and Wang, H.: Convolution Based Self Attraction and Loading in MOM6, https://doi.org/10.5281/zenodo.18445619, 2026.

Chen, J., Wilson, C., and Seo, K.-W.: S2 tide aliasing in GRACE time-variable gravity solutions, Journal of Geodesy, 83, 679–687, 2009.

Computational and Information Systems Laboratory: Derecho: HPE Cray EX System (University Community Computing), NSF: National Center for Atmospheric Research , Boulder, CO, doi:10.5065/qx9a-pg09, 2023.

Cummins, P. F. and Oey, L.-Y.: Simulation of barotropic and baroclinic tides off northern British Columbia, J. Phys. Oceanogr., 27, 762–781, 1997.

Driscoll, J. R. and Healy, D. M.: Computing Fourier transforms and convolutions on the 2-sphere, Adv. Appl. Math., 15, 202–250, 1994.

Egbert, G. D., Bennett, A. F., and Foreman, M. G.: TOPEX/POSEIDON tides estimated using a global inverse model, J. Geophys. Res.: Oceans, 99, 24 821–24 852, 1994.

Egbert, G. D., Ray, R. D., and Bills, B. G.: Numerical modeling of the global semidiurnal tide in the present day and in the last glacial maximum, J. Geophys. Res., 109, C03 003, 2004.

Erofeeva, S. and Egbert, G. D.: TPXO9-a new global tidal model in TPXO series, in: American Geophysical Union, Ocean Sciences Meeting, 186, pp. PL34C–186, 2018.

Farrell, W. E.: Deformation of the Earth by surface loads, Rev. Geophys., 10, 761–797, 1972.

Farrell, W. E.: A discussion on the measurement and interpretation of changes of strain in the Earth-Earth tides, ocean tides and tidal loading, Philosophical Transactions of the Royal Society of London. Series A, Mathematical and Physical Sciences, 274, 253–259, 1973.

Gordeev, R., Kagan, B., and Polyakov, E.: The effects of loading and self-attraction on global ocean tides: The model and the results of a numerical experiment, J. Phys. Oceanogr., 7, 161–170, 1977.

Gottlieb, D. and Shu, C.-W.: On the Gibbs phenomenon and its resolution, SIAM Rev., 39, 644–668, 1997.

Gradshteyn, I. S. and Ryzhik, I. M.: Table of integrals, series, and products, Academic press, 2014.

Greengard, L. and Rokhlin, V.: A fast algorithm for particle simulations, J. Comput. Phys., 73, 325–348, 1987.

Guo, J., Li, Y., Huang, Y., Deng, H., Xu, S., and Ning, J.: Green's function of the deformation of the Earth as a result of atmospheric loading, Geophy. J. Int., 159, 53–68, 2004.

Hendershott, M.: The effects of solid Earth deformation on global ocean tides, Geophys. J. Int., 29, 389–402, 1972.

Irazoqui Apecechea, M., Verlaan, M., Zijl, F., Le Coz, C., and Kernkamp, H.: Effects of self-attraction and loading at a regional scale: a test case for the Northwest European Shelf, Ocean Dyn., 67, 729–749, 2017.

Jayne, S. R. and St. Laurent, L. C.: Parameterizing tidal dissipation over rough topography, Geophys. Res. Lett., 28, 811–814, 2001.

Jekeli, C.: Spherical harmonic analysis, aliasing, and filtering, Journal of Geodesy, 70, 214–223, 1996.

Kang, S. K., Foreman, M. G., Lie, H.-J., Lee, J.-H., Cherniawsky, J., and Yum, K.-D.: Two-layer tidal modeling of the Yellow and East China Seas with application to seasonal variability of the M2 tide, J. Geophys. Res.: Oceans, 107, 6–1, 2002.

Le Provost, C., Genco, M., Lyard, F., Vincent, P., and Canceil, P.: Spectroscopy of the world ocean tides from a finite element hydrodynamic model, J. Geophys. Res.: Oceans, 99, 24 777–24 797, 1994.

Martens, H. R., Rivera, L., and Simons, M.: LoadDef: A Python-based toolkit to model elastic deformation caused by surface mass loading on spherically symmetric bodies, Earth and Space Science, 6, 311–323, 2019.

Merriam, J.: The series computation of the gravitational perturbation due to an ocean tide, Physics of the Earth and Planetary Interiors, 23, 81–86, 1980.

Merrifield, M. A., Holloway, P. E., and Johnston, T. S.: The generation of internal tides at the Hawaiian Ridge, Geophys. Res. Lett., 28, 559–562, 2001.

Müller, M., Haak, H., Jungclaus, J. H., Sündermann, J., and Thomas, M.: The effect of ocean tides on a climate model simulation, Ocean Modell., 35, 304–313, 2010.

Munk, W. and Wunsch, C.: Abyssal recipes II: Energetics of tidal and wind mixing, Deep Sea Res. Part I, 45, 1977–2010, 1998.

Pagiatakis, S. D.: The response of a realistic Earth to ocean tide loading, Geophys. J. Int., 103, 541–560, 1990.

Parke, M. E. and Hendershott, M. C.: M2, S2, K1 models of the global ocean tide on an elastic Earth, Mar. Geod., 3, 379–408, 1980.

Ray, R. D.: Global ocean tide models on the eve of TOPEX/POSEIDON, IEEE Trans. Geosci. Remote Sens., 31, 355–364, 1993.

Ray, R. D.: Ocean self-attraction and loading in numerical tidal models, Mar. Geod., 21, 181–192, 1998.

Rocha, C. B., Chereskin, T. K., Gille, S. T., and Menemenlis, D.: Mesoscale to submesoscale wavenumber spectra in Drake Passage, Journal of Physical Oceanography, 46, 601–620, 2016.

Sansò, F.: On the aliasing problem in the spherical harmonic analysis, Bulletin géodésique (1976-1995), 64, 313–330, 1990.

Scherneck, H.-G.: A parametrized solid Earth tide model and ocean tide loading effects for global geodetic baseline measurements, Geophys. J. Int., 106, 677–694, 1991.

Schiller, A. and Fiedler, R.: Explicit tidal forcing in an ocean general circulation model, Geophys. Res. Lett., 34, 2007.

Schrama, E. J. O.: Three algorithms for the computation of tidal loading and their numerical accuracy, Journal of Geodesy, 78, 707–714, 2005.

Schwiderski, E.: Global Ocean Tides: The semidiural principal lunar tide (M2), atlas of tidal charts and maps, Naval Surface Weapons Center, 1979.

Shriver, J., Arbic, B. K., Richman, J., Ray, R. D., Metzger, E., Wallcraft, A., and Timko, P.: An evaluation of the barotropic and internal tides in a high-resolution global ocean circulation model, Journal of Geophysical Research: Oceans, 117, 2012.

Shum, C., Woodworth, P., Andersen, O., Egbert, G. D., Francis, O., King, C., Klosko, S., Le Provost, C., Li, X., Molines, J.-M., et al.: Accuracy assessment of recent ocean tide models, J. Geophys. Res.: Oceans, 102, 25 173–25 194, 1997.

Simpson, J. H. and Hunter, J.: Fronts in the Irish sea, Nature, 250, 404–406, 1974.

Stammer, D., Ray, R. D., Andersen, O. B., Arbic, B. K., Bosch, W., Carrere, L., Cheng, Y., Chinn, D. S., Dushaw, B. D., Egbert, G. D., et al.: Accuracy assessment of global barotropic ocean tide models, Rev. Geophys., 52, 243–282, 2014.

Stepanov, V. N. and Hughes, C. W.: Parameterization of ocean self-attraction and loading in numerical models of the ocean circulation, J. Geophys. Res.: Oceans, 109, 2004.

Thomas, M., Sündermann, J., and Maier-Reimer, E.: Consideration of ocean tides in an OGCM and impacts on subseasonal to decadal polar motion excitation, Geophys. Res. Lett., 28, 2457–2460, 2001.

Wang, H., Xiang, L., Jia, L., Jiang, L., Wang, Z., Hu, B., and Gao, P.: Load Love numbers and Green's functions for elastic Earth models PREM, iasp91, ak135, and modified models with refined crustal structure from Crust 2.0, Comput. Geosci., 49, 190–199, 2012.

Wang, H., Hallberg, R., Wallcraft, A. J., Arbic, B. K., and Chassignet, E. P.: Improving global barotropic tides with sub-grid scale topography, J. Adv. Model. Earth Syst., 16, e2023MS004 056, 2024.

Waterhouse, A. F., MacKinnon, J. A., Nash, J. D., Alford, M. H., Kunze, E., Simmons, H. L., Polzin, K. L., St. Laurent, L. C., Sun, O. M., Pinkel, R., et al.: Global patterns of diapycnal mixing from measurements of the turbulent dissipation rate, J. Phys. Oceanogr., 44, 1854–1872, 2014.